



HAL
open science

The real potential of current passive satellite data to map aboveground biomass in tropical forests

Nidhi Jha, Nitin Kumar Tripathi, Nicolas Barbier, Salvatore G. P. Virdis, Wirong Chanthorn, Gaëlle Viennois, Warren Brockelman, Anuttara Nathalang, Sissades Tongsimma, Nophea Sasaki, et al.

► To cite this version:

Nidhi Jha, Nitin Kumar Tripathi, Nicolas Barbier, Salvatore G. P. Virdis, Wirong Chanthorn, et al.. The real potential of current passive satellite data to map aboveground biomass in tropical forests. *Remote Sensing in Ecology and Conservation*, 2021, 7 (3), pp.504-520. 10.1002/rse2.203 . hal-03193170

HAL Id: hal-03193170

<https://hal.inrae.fr/hal-03193170>

Submitted on 8 Apr 2021

HAL is a multi-disciplinary open access archive for the deposit and dissemination of scientific research documents, whether they are published or not. The documents may come from teaching and research institutions in France or abroad, or from public or private research centers.


L'archive ouverte pluridisciplinaire **HAL**, est destinée au dépôt et à la diffusion de documents scientifiques de niveau recherche, publiés ou non, émanant des établissements d'enseignement et de recherche français ou étrangers, des laboratoires publics ou privés.



Distributed under a Creative Commons Attribution - NonCommercial - NoDerivatives 4.0 International License

ORIGINAL RESEARCH

The real potential of current passive satellite data to map aboveground biomass in tropical forests

Nidhi Jha^{1,2,3} , Nitin Kumar Tripathi¹, Nicolas Barbier², Salvatore G. P. Virdis¹, Wirong Chanthorn⁴, Gaëlle Viennois², Warren Y. Brockelman³, Anuttara Nathalang³, Sissades Tongsima³, Nophea Sasaki⁵, Raphaël Pélissier² & Maxime Réjou-Méchain²

¹Department of Information & Communication Technologies, School of Engineering and Technology (SET), Asian Institute of Technology, Pathum Thani, Thailand

²AMAP, Univ Montpellier, IRD, CNRS, CIRAD, INRAE, Montpellier, France

³National Biobank of Thailand, National Science and Technology Development Agency (NSTDA), Science Park, Pathum Thani, Thailand

⁴Faculty of Environment, Kasetsart University, Bangkok, Thailand

⁵Department of Development and Sustainability, School of Environment, Resources and Development (SERD), Asian Institute of Technology, Pathum Thani, Thailand

Keywords

Biomass mapping, forest carbon, passive satellite sensor, random forest, sensor saturation limit

Correspondence

Nidhi Jha, National Biobank of Thailand, National Science and Technology Development Agency (NSTDA), Science Park, Pathum Thani, Thailand. Tel: +66 (0) 909923705; Fax: +66 (0) 2-564-7001; E-mail: nidhi23aug@gmail.com

Editor: Mat Disney

Associate Editor: José Hernández-Stefanoni

Received: 1 October 2020; Revised: 6 March 2021; Accepted: 12 March 2021

doi: 10.1002/rse2.203

Abstract

Forest biomass estimation at large scale is challenging and generally entails large uncertainty in tropical regions. With their wall-to-wall coverage ability, passive remote sensing signals are frequently used to extrapolate field estimates of forest aboveground biomass (AGB). However, studies often use limited reference data and/or flawed validation schemes and thus report unreliable extrapolation error estimates. Here, we compared the ability of three medium- to high-resolution passive satellite sensors, Landsat-8 (L8), Sentinel-2B (S2) and Worldview-3 (WV3), to map AGB in a forest landscape of Thailand. We used a large airborne LiDAR-derived AGB dataset as a reference to train and validate a random forest algorithm and conducted robust error assessments and variable selection using spatialized cross-validations. Our results indicate that the selected predictors strongly varied among the three sensors and between analyses were restricted to low (≤ 200 Mg ha⁻¹) and high (> 200 Mg ha⁻¹) AGB areas. WV3 and S2 data outperformed L8 data to extrapolate AGB (RMSE of 68 and 72 against 84 Mg ha⁻¹, respectively) due to the inclusion of the red-edge band and, probably, to their higher spatial and spectral resolution. Sensitivity to large AGB values was higher for WV3 than for S2 and L8 with saturation point of 247 Mg ha⁻¹ against 204 and 192 Mg ha⁻¹. AGB values above these saturation points remained poorly predictable, especially for L8, indicating that several tropical forest AGB maps should be interpreted with extreme caution. However, predicted gradients of lower AGB values (≤ 200 Mg ha⁻¹), i.e., in early forest successional stages, were fairly consistent among sensors ($r > 0.70$), even if the mean absolute difference between estimates was large when AGB predictions were extrapolated out of the calibration area at regional level (34%). We finally showed that calibrating the model only within the sensitivity AGB domain (e.g., < 200 Mg ha⁻¹) minimizes the risk of induced bias for estimating small AGB values. These results provide important benchmarks for interpreting previously published maps and to improve future validation schemes.

Introduction

Tropical forests store large amounts of terrestrial carbon and thus play a significant role in the global carbon budget (Pan et al., 2011). However, the amount of carbon stocks stored in these high-biomass forests remains highly uncertain (Mitchard et al., 2013). Forest aboveground biomass (AGB), a proxy for carbon stock, is often estimated from field-based measurements that are upscaled with the help of passive or/and active remote sensing (RS) data (Berninger et al., 2018; Réjou-Méchain et al., 2019). Many RS data sources have been proposed as candidates for extrapolating forest AGB in the tropics, including multispectral high (e.g., RapidEye or Worldview; Bastin et al., 2014; Ploton et al., 2013) to medium and coarse (e.g., Sentinel-2, Landsat or MODIS; Avitabile et al., 2012; Baccini et al., 2008, 2012; Ghosh & Behera, 2018; Saatchi et al., 2011) resolution. However, these studies often faced two common problems. First, the somewhat limited number of field data used to calibrate the RS model may result in important model calibration errors and in poor ability to capture the full spectrum of vegetation heterogeneity (Marvin et al., 2014). Second, the use of flawed validation schemes, where non-spatially independent observations are used for validation, lead to overly optimistic prediction errors (Ploton et al., 2020). These two limitations generally result in poor understanding of the functional relationship between RS signals and forest AGB and in a poor ability to quantify uncertainties in AGB mapping.

Airborne Light Detection and Ranging (LiDAR) captures detailed spatial variations in forest structure and hence has proven to be a reasonably accurate alternative for scaling up a limited number of field data estimates to landscape-scale with a 10%–15% accuracy at 1-ha resolution (Zolkos et al., 2013). However, due to the high acquisition cost of airborne LiDAR data, extrapolation areas are often restricted to relatively small spatial coverage (typically less than 100 km²; Silva et al., 2017). LiDAR-derived AGB estimates have thus been proposed as a key intermediate product between field and satellite-based data with a two-step upscaling strategy consisting of first calibrating an intermediate-scale AGB map using field and LiDAR data, and then using this map as a reference to calibrate satellite images of coarser resolution and broader swath (Asner et al., 2013; Baccini & Asner, 2013; Baccini et al., 2012; Sagang et al., 2020; Xu et al., 2017). This two-step strategy has several advantages, such as considerably improving the representativeness and number of calibration and validation data (Marvin et al., 2014), minimizing the spatial mismatch that may arise between field and satellite data (Mascaro et al., 2011; Réjou-Méchain et al., 2019) and providing enough data to design robust calibration and validation schemes, accounting for spatial autocorrelation (Ploton et al., 2020).

Sensitivity to forest AGB of the many RS predictors derived from passive satellite proposed in the literature, remains poorly known/evaluated, especially in dense forests. It has already been shown that many satellite-derived vegetation indices widely used for predicting forest AGB in temperate and boreal forests saturate at higher AGB values of typically >150 Mg ha⁻¹ (Meyer et al., 2019; Mutanga & Skidmore, 2004). Nevertheless, new freely available products such as Sentinel-2 multispectral instrument (MSI) with three bands in the red-edge and higher spatial resolution (10 m against 30 m for Landsat) may increase our capabilities to map forest AGB (Chang & Shoshany, 2016; Malenovsky et al., 2012). Until recently, the upscaling potential of Sentinel 2 data has been little investigated for tropical forests. Finally, in addition to spectral bands and band ratios, several studies have demonstrated that texture indices from high to very high-resolution images have a good potential for estimating forest AGB with no saturation at high AGB values (Couteron et al., 2015; Pargal et al., 2017; Ploton et al., 2017). At such a fine resolution, the information extracted from the distribution of tree crown sizes may indeed correlate well with forest AGB (Couteron et al., 2015; Tuominen & Pekkarinen, 2005).

Several studies have attempted to assess the saturation limit of different satellite data for estimating forest AGB (Li et al., 2019; Lu et al., 2016; Mermoz et al., 2015; Zhao et al., 2016). However, only a few studies have compared the saturation limits of different sensors using a large AGB reference dataset, such as LiDAR-AGB data, with spatially independent observations for validation. This study was designed to assess and compare the AGB prediction potential of multi-resolution passive RS products in a tropical forest landscape. We used a recently published 60-km² LiDAR-AGB map as a reference to assess the predictive power of multispectral bands, and their derived spectral and textural indices, from three different space-borne sensors: Landsat-8, Sentinel-2B and Worldview-3. Specifically, this study aims to (i) determine the relative predictive power and range of sensitivity of these medium- to high-resolution satellite data using spatially independent observations for validation; (ii) identifying the raw bands and their derived indices that best predict low and, possibly, high forest AGB values; and (iii) discussing the implications of the use of current passive satellite data for mapping aboveground biomass and carbon in tropical forests.

Materials and Methods

Study area

The study area is located in Khao Yai National Park (KYNP), which covers over 2000 km² in central Thailand

(14° 25' 20.4" N, 101° 22' 36.9" E; Fig. 1). KYNP is the first national park of Thailand, established in 1962. The altitude of the national park ranges from 100 to 1350 m. The forest of interest consists of seasonal evergreen forest that lies between approximately 700 and 900 m altitude, which covers roughly half of the park area. This forest annually receives approximately 2200 mm of precipitation with annual mean temperature of about 23°C (Jenks et al., 2011), and has a dry season of 5–6 months (Brockelman et al., 2017). Below 700 m the park contains semi-evergreen and deciduous forests, some highly degraded, and above 900 m the forest grades into wetter, lower montane forest of lower stature. The study area within the seasonal evergreen forest zone consists of a mosaic of mature and secondary forests of different successional stages (Chanthorn et al., 2017; Jha et al., 2020).

Data preparation

Airborne LiDAR-derived and field AGB data

Airborne LiDAR-derived AGB values are those produced in Jha et al. (2020). In brief, airborne LiDAR data were acquired at very high density (>25 pts m^{-2}) using a RIEGL LMS Q680i on 10 April 2017 on ca. 64 km^2 of forest area located in the northern part of KYNP (Fig. 1). We additionally used 70 field plots (each approximately 0.5 ha) belonging to different successional stages (from young- to old-growth forests) where all trees >5 cm in diameter were censused using a protocol developed by the FORESTGEO-CTFS network (Jha et al., 2020). AGB at the field plot level was estimated by summing individual tree AGB estimates for all trees using the pantropical allometric model of Chave et al. (2014) through the BIOMASS R package (Réjou-Méchain et al., 2017). Field plot AGB values ranged from 80 to about 580 $Mg\ ha^{-1}$ with an average of 315 $Mg\ ha^{-1}$ LiDAR top-of-canopy height (TCH) was calibrated against the 70-field plot AGB estimates through a log-log linear model to produce a LiDAR-AGB map at 60-m resolution with an associated error of 45 $Mg\ ha^{-1}$ (14%) (Jha et al., 2020).

Passive earth observation satellite data

We used three different sources of passive multispectral satellite data: Landsat-8 (L8), Sentinel-2B (S2) and Worldview-3 (WV3). The characteristics of the images and bands used are summarized in Table 1. For L8 and S2, data were acquired during the dry season (November to April) to minimize cloud cover. Atmospheric correction and dehazing were carried out on orthorectified and radiometrically calibrated products and the bottom-of-atmosphere (BoA) reflectance was computed using the Overland image processing software (developed by Airbus

Defense and Space; Feret & Barbier, 2018). The different image tiles were mosaicked to cover the whole KYNP area.

We also used a high-resolution WV3 image fully covering the LiDAR area, but given its prohibitive cost, we did not purchase WV3 data over the whole of KYNP area. From the ortho-ready product, we performed the orthorectification using rational polynomial coefficients (accuracy < 0.3 m), the LiDAR digital surface model and ground control points. Due to administrative issue the WV3 was acquired just before rainy season i.e., June 2018 instead of dry season but the image contained less than 15% cloud cover, which was masked in subsequent analyses. To make the three images radiometrically comparable, the digital number values of the original WV3 images were calibrated and converted to the BoA reflectance values.

The pre-processed L8, S2 and WV3 images were resampled at 60-m pixel size resolution for comparing the upscaling potential of the three datasets at the same scale and to match the LiDAR-derived AGB map. The main reason for aggregating all data to 60-m was to minimize the edge effects and potential geolocation errors that strongly blur the forest AGB-RS signal at smaller scales in tropical forests (Mascaro et al., 2011; Réjou-Méchain et al., 2019).

To maximize the comparison between sensors, all analyses were conducted only considering the WV3 cloud- and shadow-free pixels.

Remote sensing predictors

We used 37–57 AGB predictors according to the data source, including the original aggregated bands, intra 60-m pixel statistics based on bands at original resolution and derived multispectral or textural indices (Table 2). These predictors were chosen from the literature, following their claimed capability to predict AGB. We categorized predictors into three groups: multispectral bands, spectral metrics and intrapixel metrics.

We used several spectral metrics and, depending on the expected physiological processes captured, categorized them as vegetation indices (VIs) and Biophysical variables (BVs). VIs (indices 1–11 in Table 2) enhances the spectral features sensitive to vegetation density while reducing noise due to soil or atmosphere effects (Clevers, 2014). They are therefore expected to correlate with AGB but are also well-known to saturate rapidly with increasing AGB values (Baloloy et al., 2018). In order to minimize this problem, we also used modified vegetation indices where Red band is replaced by the Red-edge band (Zhang et al., 2017).

BVs (indices 12–16 in Table 2) are also expected to relate to the vegetation status, mainly through its

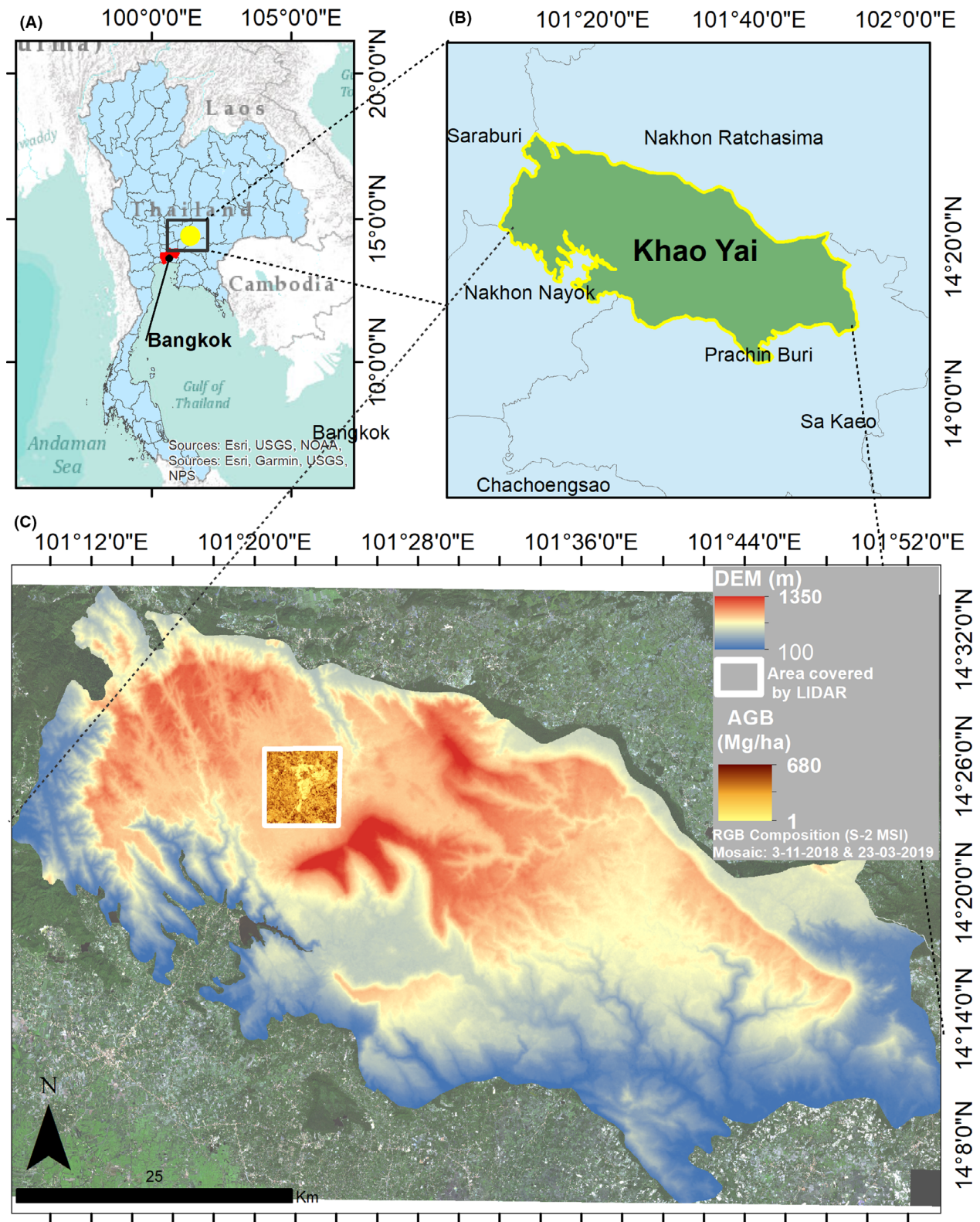


Figure 1. Study area. (A) Location of the study area in Thailand (in yellow); (B) location of Khao Yai National Park; (C) digital elevation model (DEM) of the total area of Khao Yai National park with the location of the LiDAR scene (in white frame) with AGB values at 60-m resolution.

Table 1. Characteristics of passive earth observation satellite data.

	Landsat-8	Sentinel-2	Worldview-3
Data download source	USGS http://glovis.usgs.gov	PEPS https://peps.cnes.fr/rocket/	Purchased from Digital Global
Data catalogue	WRS-2 path/row: 129/50 & 128/50	47 PQS; 47PQR; 47 PRR	
Sensor	OLI & TIRS	MSI	–
Spatial Coverage	2170 km ²	2170 km ²	113 km ²
No. of images	2	2	1
Date	5/11/2018 & 14/12/2018	3/11/2018 & 23/03/2019	23/06/2018
Spatial resolution	30 m	10 m	MSS-1.2 m/Pan 0.3 m (used for Texture)
Bands with associated spectral range mean in micrometers	B2 Blue _{0.483} , B3 Green _{0.560} , B4 Red _{0.660} , B5 NIR _{0.865} , B6 SWIR-1 _{1.650} , B7 SWIR-2 _{2.220}	B2 Blue _{0.490} , B3 Green _{0.560} , B4 Red _{0.665} , B5 Red-edge1 _{0.705} , B6 Red-edge2 _{0.740} , B7 Red-edge3 _{0.783} , B8 NIR1 _{0.842} , B8A NIR narrow or Vegetation Red Edge _{0.865} , B11 SWIR-1 _{1.610} , B12 SWIR-2 _{2.190}	B1CoastalBlue _{0.426} , B2Blue _{0.481} , B3Green _{0.547} , B4Yellow _{0.605} , B5Red _{0.661} , B6Red-edge _{0.725} , B7NIR1 _{0.832} , B8NIR2 _{0.948}

chlorophyll content (Widłowski et al., 2004). The chlorophyll content of a forest stand is indeed expected to correlate, at least partially, with AGB (Boutton et al., 1988; Keeler et al., 2015). The wavelength regions most sensitive to chlorophyll pigment variation lie between 550 nm (i.e., green) and 715 nm (Red-edge); hence, these two bands were used to enhance chlorophyll factors (Baloloy et al., 2018).

Finally, to utilize the full potential and the information provided by the original resolution of the three sensors, we computed 60-m intrapixel statistics. For the three sensors, we calculated the standard deviation, coefficient of variation and homogeneity of all the available bands at their original spatial resolution. Due to the high-resolution nature of WV3, we additionally derived image texture variables from the panchromatic band of the WV3 image using 60-m windows (indices 17–18 in Table 2). We used the Fourier Transform Textural Ordination (FOTO), an unsupervised analysis aimed at extracting features from high-resolution images, to describe canopy characteristics, such as crown size and heterogeneity (Couteron et al., 2005; Ploton et al., 2012). As suggested by Ploton et al. (2016), we additionally computed lacunarity texture variables that are directly sensitive to canopy gaps. We used the first three axes of independent Principal Component Analyses, performed on the table of Fourier r-spectra on the one hand and lacunarity spectra on the other hand (indices 17–18 in Table 2).

Therefore, in total, we used as candidates for the AGB prediction model 37 variables for L8 data, 57 variables for S2, and 52 variables for WV3, hereafter, referred to as RS predictors. We additionally added as a predictor the elevation (30-m resolution) from the Shuttle Radar Topography Mission (SRTM) because topography has an

impact on water and nutrient availability and is known to strongly impact forest AGB variation (Réjou-Méchain et al., 2014).

Statistical model

We used a Random Forest (RF) machine-learning algorithm to predict LiDAR-derived AGB values from several predictors selected through a robust selection procedure. The RF algorithm accounts for non-linear relationships between predictors and the response variable, as well as for interactions between predictors. This approach has been shown to be very efficient (Mascaro et al., 2014), especially when RS data have a strong sensitivity to a large range of AGB, and when the training data are numerous, independent and widespread across the area of interest (Meyer et al., 2019). However, RF is known to be highly subject to the overfitting and is strongly influenced by spatial autocorrelation among observations (Ploton et al., 2020). We thus adopted a leave-one-block-out (LOBO) cross-validation approach, as increasingly recommended to minimize spurious autocorrelation effects (Ploton et al., 2020; Roberts et al., 2017), where the whole LiDAR-derived AGB map was divided into four independent spatial blocks of ca. 1200 ha each. This approach consisted in (i) first fitting each RF model with three blocks of training data, leaving one block for validation, (ii) then using the model to predict the observations held out of model calibration. The process of spatial cross-validation was repeated for all four sets of blocks to improve model prediction accuracy. Here, we assessed accuracy with the root mean square error (RMSE), that is independently evaluated from all the four blocks (hereafter referred to as LOBO-RMSE criterion). A spatial

Table 2. Summary of some predictor variables. The variable used in each sensor is marked by x.

S. No	Variables	Equations	Variables derived from Sensors			References
			L8	S2	WV3	
1	Normalized difference vegetation index (NDVI)	$\frac{NIR-Red}{NIR+Red}$	x	x	x	Tucker (1979)
2	Transformed NDVI (TNDVI)	$\sqrt{NDVI} + 0.5$	x	x	x	Tucker (1979)
3	Pan NDVI (PNDVI)	$\frac{NIR-(Green+Red+Blue)}{NIR+(Green+Red+Blue)}$	x	x	x	Wang et al. (2007)
4	Wide dynamic range vegetation Index (WDRVI)	$\frac{(0.1+NIR)-Red}{(0.1+NIR)+Red}$	x	x	x	Gitelson (2004)
5	Green NDVI (GNDVI)	$\frac{(NIR-Green)}{(NIR+Green)}$	x	x	x	Gitelson et al. (1996)
6	Normalized difference water index (NDWI)	$\frac{Green-NIR}{Green+NIR}$	x	x	x	(McFeeters, 1996)
7	Normalized burn ratio (NBR)	$\frac{NIR-SWIR}{NIR+SWIR}$	x	x		Miller and Thode (2007)
8	Normalized difference red edge or NDVI red edge (NDRE)	$\frac{NIR1-Red\ Edge\ 1}{NIR1+Red\ Edge\ 1}$		x	x	Sims and Gamon (2002)
9	Moisture index (MI)	$\frac{NIR2-SWIR}{NIR2+SWIR}$		x		Gao (1995)
10	Green vegetation index MSS (GVIMSS)	$-0.283 - 0.660 + 0.577Red\ Edge + 0.388NIR2$		x	x	Bannari et al. (1995)
11	Specific leaf area vegetation index (SLAI)	$\frac{NIR}{Red+SWIR}$	x	x		Lymburner et al. (2000)
12	Chlorophyll green (Cgreen)	$\left(\frac{NIR}{Green}\right)^{-1}$	x	x	x	Gitelson et al. (2006)
13	Chlorophyll index green (Clgreen)	$\left(\frac{NIR}{Green}\right) - 1$	x	x	x	(Gitelson, 2004)
14	Chlorophyll index red/red-edge (Clred)	$\left(\frac{NIR}{RedorRedEdge}\right) - 1$	x	x	x	Gitelson (2004)
15	Chlorophyll vegetation index (CVI)	$NIR\left(\frac{Red}{Green^2}\right)$	x	x	x	Vincini et al. (2008)
16	Leaf chlorophyll index (LCI)	$\frac{NIR2-Red}{NIR2+Red}$		x	x	Pu et al. (2008)
17	FOTO (texture)	PCA axes 1 to 3			x	Coueron et al. (2005)
18	Lacu (texture, lacunarity)	PCA axes 1 to 3			x	Ploton et al. (2017)
19	DEM (23/09/2014) (SRTM)		x	x	x	Rodríguez et al. (2006)

variogram analysis performed on LiDAR predicted AGB values revealed that AGB is not anymore spatially aggregated above 3000 m in our study area (Fig. S1) so that dividing our study area into four blocks of 3464×3464 m using iteratively data from one block to validate the model trained from data belonging to the three other blocks generates validation data that are both statistically and spatially independent of the calibration data. As the variable importance index provided by RF derives from internal Out-of-Bag procedures that do not account for spatial dependence in observations, we designed a forward selection procedure that starts by selecting the best discriminant variable according to the LOBO-RMSE criterion. The process then continues by selecting the second-best discriminant variable, and so on. We finally kept only predictive variables that contributed to a decrease of absolute RMSE by more than 1 Mg ha^{-1} to minimize any model overfitting that would occur by chance. To assess the overall gain of our final selected RF model, we compared it with a null model containing all predictors but where AGB values were randomized during

the model calibration stage. This process was repeated fifty times to provide the mean and standard deviation of the fifty RMSE values expected under the null model.

We additionally assessed the sensitivity of each sensor to predict AGB above and below to an arbitrary threshold of 200 Mg ha^{-1} . To do this, we repeated the calibration/validation and variable selection steps described above independently for each sensor but restricting the analyses to areas where the LiDAR-derived AGB values were either below (1652 ha) or above (3,561 ha) 200 Mg ha^{-1} and compared the LOBO-RMSE criterion among sensors.

Sensor comparisons

Signal sensitivity to forest AGB

For each sensor, we independently assessed the signal saturation point, i.e., the AGB value above which a marked decrease in sensitivity of signal to AGB is observed (Joshi et al., 2017). To identify this signal saturation point, we

used the observed values and the predicted ones, obtained from the LOBO cross-validation approach, and fitted a piecewise linear regression model. This regression approach allows the detection of a breaking point in a linear relationship. In order to facilitate cross-sensor comparisons, we selected only one breaking point and used 1000 bootstrap replicates to estimate its 95% confidence interval (CI).

We then used the Pearson's correlation (r) between observed and predicted AGB to quantify the model predictive power below and above the signal saturation point.

Inter-sensors comparison

We compared the AGB predicted by different sensors through a standard major axis (SMA) regression approach. Contrary with classic ordinary least-squares (OLS) regression, which assumes that only Y values have associated errors, SMA accounts for errors in both X and Y and thus does not assume any hierarchy between the two variables.

Variable transferability among sensors

The best predictors of forest AGB may vary from sensor to sensor (Brosofske et al., 2014). In order to identify the most universal or transferable AGB predictors across sensors, we repeated the LOBO-RMSE selection procedure considering only the common variables ($n = 15$) among the three sensors.

AGB extrapolation to the whole study area

We finally compared the AGB prediction from L8 and S2 data at the scale of the KYNP, hence outside the calibration area, using a SMA regression model between AGB values predicted by both sensors. This analysis did not aim at assessing the accuracy of the extrapolated values, because no validation data were available outside our LiDAR area, but to understand how consistent were the S2 and L8 predicted AGB values when extrapolated regionally, out of the calibration area, as it would be done for any large-scale prediction study.

All statistics in this study were performed using the random Forest package (Liaw & Wiener, 2002) of the R software version 3.6.1 (<https://www.r-project.org/>).

Results

Selection of the predictors

Our selection procedure retained four to five predictors for each sensor (the addition of other variables did not

reduce the LOBO-RMSE by more than 1 Mg ha^{-1} ; Fig. 2). Scatterplots between LiDAR-derived AGB values and the selected predictors taken individually are given in the Figures S2–S4. Our spatial cross-validation approach showed that the selected predictors for L8, S2 and WV3 predicted LiDAR-derived AGB values with an RMSE of ca. 84 Mg ha^{-1} (29%), 72 Mg ha^{-1} (24%) and 68 Mg ha^{-1} (23%), respectively (Table S1). We also assessed the sensitivity of different satellite sensors for predicting low ($\leq 200 \text{ Mg ha}^{-1}$) and high ($> 200 \text{ Mg ha}^{-1}$) AGB values (Fig. S5). As expected, our spatial cross-validation approach revealed that, for all satellite sensors, AGB values $\leq 200 \text{ Mg ha}^{-1}$ were much more accurately predicted ($r = 0.65$ – 0.79 ; relative RMSE of 19%–24%, compared to 28% with the null model) than AGB values $> 200 \text{ Mg ha}^{-1}$ ($r = 0.09$ – 0.36 ; relative RMSE of 21%–25%, compared to 31% with the null model). S2 and WV3 tended to provide more accurate estimates for both low and high AGB values than L8. The number of selected predictors was smaller for low AGB values (2–3) than for high AGB values (4–5). The Green band_{0.560} (B3) of L8, the Red-edge band_{0.705} (B5) of S2, and the NDRE index of WV3 were independently retained as the best predictors for low AGB values, with correlations with the LiDAR-derived AGB gradient below to 200 Mg ha^{-1} , of -0.62 , -0.78 and 0.78 , respectively (Fig. S6). The best predictor for the AGB gradient above $> 200 \text{ Mg ha}^{-1}$ for L8, S2 and WV3 sensors were Green band_{0.560} (B3), GVIMSS index and Red-edge band_{0.725} (B6), respectively, with independent correlations shown in Figure S7.

Functional form of satellite-derived AGB models

We found that the signal saturation points varied among satellite datasets and were ca. 192 Mg ha^{-1} (95% CI 185–197) for L8, 204 Mg ha^{-1} (95% CI 200–209) for S2, and 247 Mg ha^{-1} (95% CI 240–255) for WV3 data (Fig. 3). Above these thresholds, all datasets exhibited significant, albeit weak, correlations between observed and predicted datasets, but with a better performance of S2 and WV3 data compared to L8 data. For all data sources, the models tended to overestimate small AGB values and strongly underestimate large AGB values.

Sensor comparisons

Inter-sensors comparisons

The comparison of the paired predicted AGB values by the different sensors indicated relatively good overall agreement, especially for low AGB values (Fig. 4). For higher AGB values ($> 250 \text{ Mg ha}^{-1}$), the highest, albeit

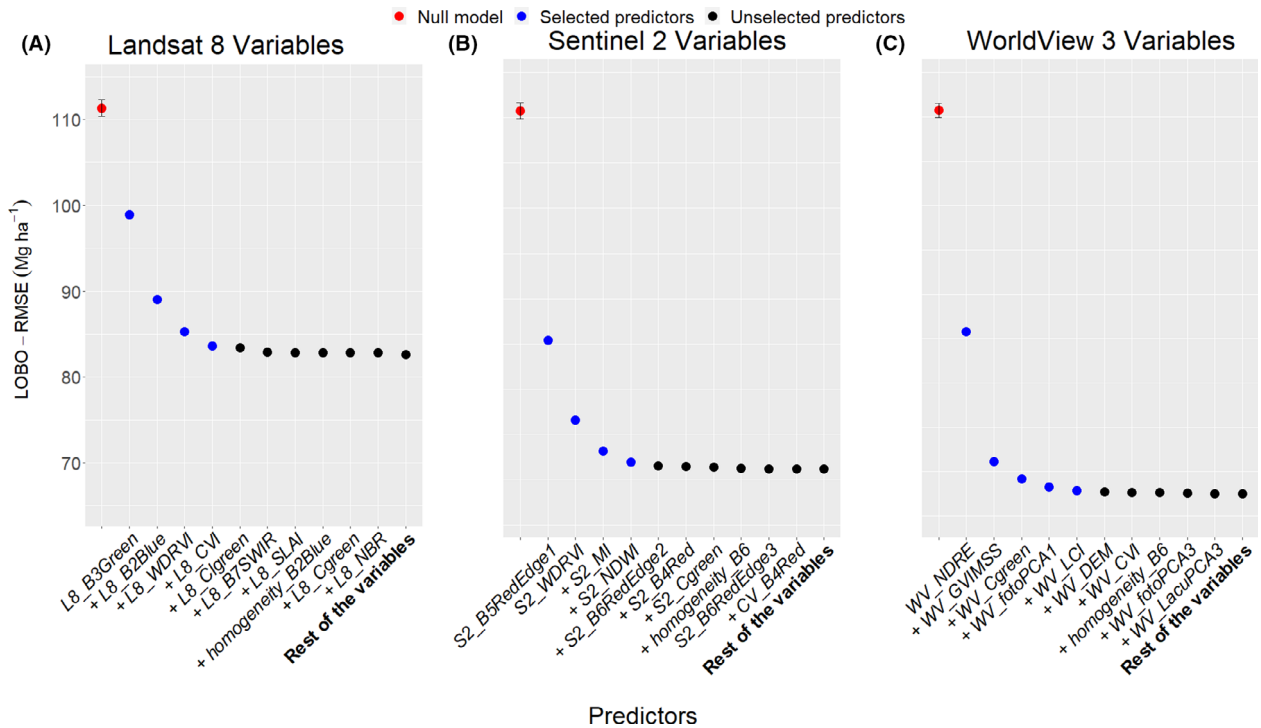


Figure 2. Selection of sensor predictors using both a leave-one-block-out (LOBO) cross-validation approach and a forward selection for the three satellite datasets (A–C). The first selected predictor is the one contributing to the highest decrease in LOBO-RMSE, and then additional predictors are added to the model using the same rule. Only predictors contributing to a decrease of more than 1 Mg ha⁻¹ in the LOBO-RMSE are selected in the final model (in blue). The expected LOBO-RMSE under a null model, i.e., breaking the link between forest AGB and RS signal, is represented by a red dot.

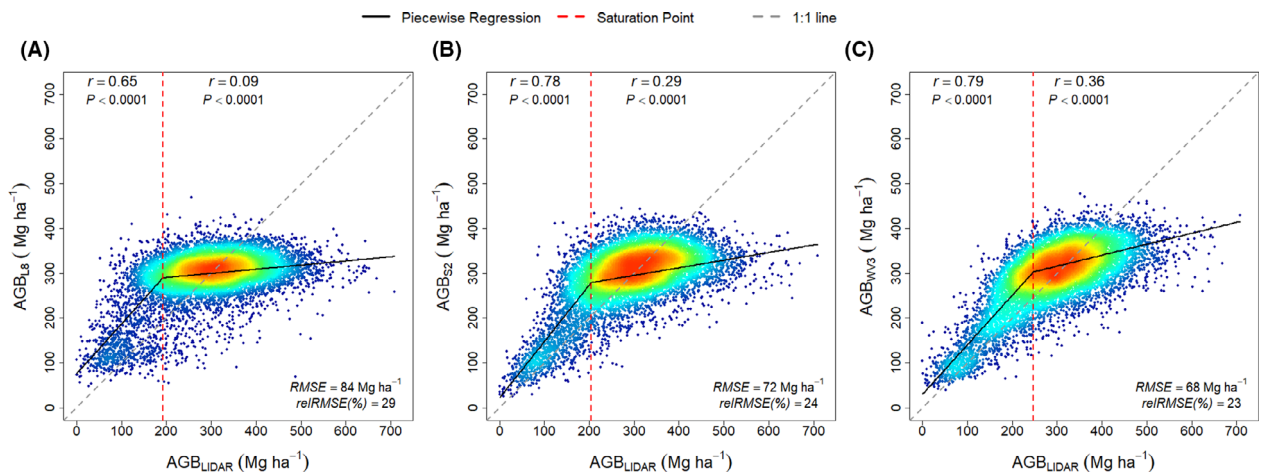


Figure 3. Predicted and observed (LiDAR) AGB for the three satellite datasets obtained from a leave-one-block-out cross-validation approach (A) L8 predicted AGB versus LiDAR-derived AGB (B) S2 predicted AGB versus LiDAR-derived AGB; (C) WV3 predicted AGB versus LiDAR-derived AGB. Pearson’s r correlation coefficient and associated P values for each piecewise regression segment are reported within each panel. Blue to red colour indicates low to high point density, respectively.

weak, correlations were observed between L8 and S2 predictions and between WV3 and S2 predictions ($r = 0.33$ and 0.31 , respectively, $P < 0.0001$). By contrast, WV3

predictions for these large AGB values were comparatively poorly correlated with L8 predictions ($r = 0.16$). The SMA regression showed significant departures from the

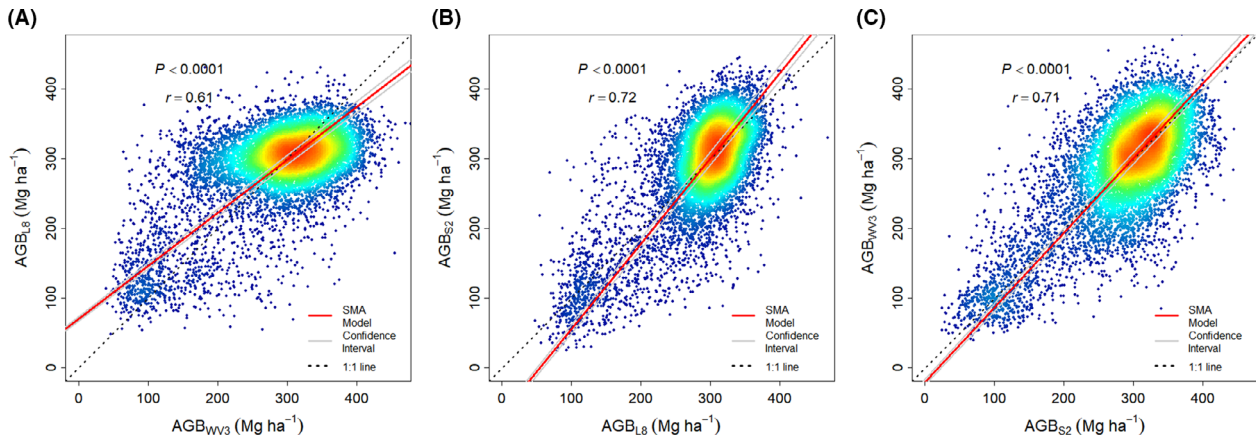


Figure 4. Relationship between predicted AGB values from the three datasets (A) Landsat-8 and Worldview-3 (B) Sentinel-2 and Landsat-8 (C) Worldview-3 and Sentinel-2. Blue to red colour indicates low to high point density, respectively.

1:1 line but did not reveal any major bias between sensor predictions.

Variable transferability among sensors

The common selection procedure, based on the mean LOBO-RMSE among the three sensor datasets, resulted in five selected predictors: the Green, Blue and Red bands, and the GNDVI and PNDVI indices (Fig. 5). The resulting prediction errors were 84, 77 and 71 Mg ha⁻¹ for L8, S2 and WV3, respectively, indicating that the higher

potential of WV3 and S2 is not only due to the availability of other bands, but is also marked when similar spectral regions and indices are used.

Extrapolation to the regional scale

Using the predictors independently selected from S2 and L8 data, we predicted AGB over the whole KYNP area at the 60-m resolution, but with a unique open class for pixels ≥200 Mg ha⁻¹ because of signal saturation (Fig. 6). The overall correlation coefficient between the two

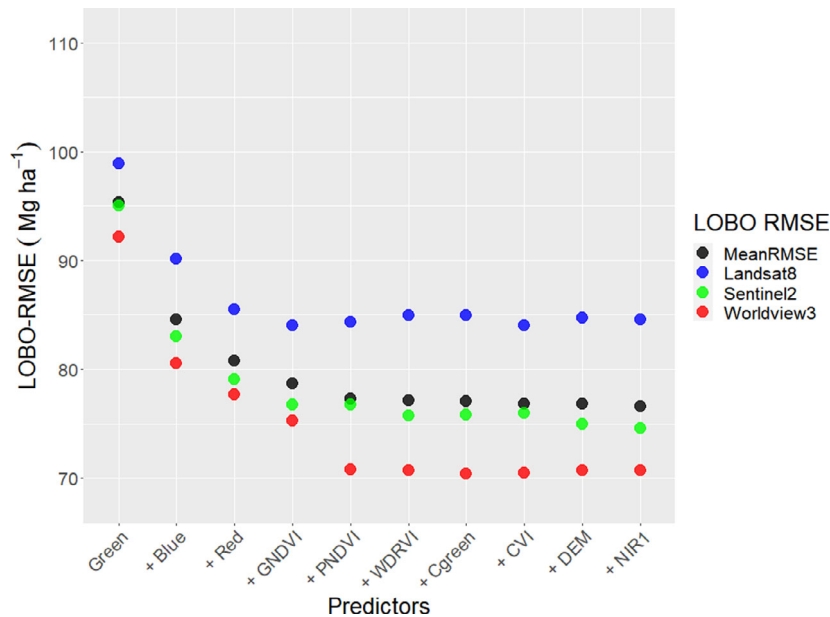


Figure 5. Selection of the best predictors common to the three satellite datasets. The method is the same as that used for Figure 2, but here, predictors are selected based on the mean of the three sensor-specific LOBO-RMSE values. The first five predictors are chosen based on our criteria for selecting variables that contributed to a decrease in mean RMSE by more than 1 Mg ha⁻¹.

estimates was 0.56, but L8 predictions were, on average, 34% higher than S2 predictions, resulting in estimates of total AGB stock for these low AGB areas of 18.02 Tg (teragrams) and 11.81 Tg, respectively. WV3, which provided the most accurate local estimates, was not available over the full extent.

Discussion

In this paper, we used imagery from three different satellite sensors to assess their potential to map AGB at a large scale in a heterogeneous dense forest area. Using both a large LiDAR dataset and robust statistical procedures controlling for spatial autocorrelation, we showed that higher resolution products such as WV3 and S2 provide more accurate AGB predictions than L8 data in a tropical forest landscape. As discussed below, this higher accuracy may originate from both the higher spatial and spectral resolution of WV3 and S2 data compared to L8, and the availability of the Red-edge band. Globally, predictions of low AGB values ($\leq 200 \text{ Mg ha}^{-1}$) were fairly consistent among sensors, even if systematic differences of nearly 34% were observed when we extrapolated the predictions over the full region of interest.

The relative potential of passive remote sensing data to map forest AGB

As expected, we found that predictors from the three satellite sensors conveyed important information on forest AGB variation, at least for low AGB values ($\leq 200 \text{ Mg ha}^{-1}$). For these low AGB values, the three datasets provided consistent predictions ($r > 0.70$), with an error ranging from 19% to 24%, and did not show major systematic differences in paired predictions. For higher AGB values, L8 provided almost no information while S2 and WV3 showed modest correlations ($r > 0.3$) between observations and predictions. More generally, we also found a significantly higher potential of WV3 and S2 data to predict AGB values, compared to L8 data, even when analyses were restricted to common bands (Fig. 5). Four reasons may explain this higher potential. First, as can be seen by comparing the analyses based on all variables (Fig. 2) and restricted to common variables (Fig. 5), the Red-edge bands from S2 and WV3, absent from L8, significantly improved prediction accuracy. The Red-edge region is located in a transitional reflectance region, between Red band and NIR region (Horler et al., 1983), and thus has potentially good sensitivity to forest structure (Gitelson, 2004). Second, the higher spatial resolution of these products, compared to L8, may allow capturing more subtle AGB variation, even in high AGB areas. Third, the higher resolution also led to a higher

number of pixels aggregated at the mapping resolution (60 m), thereby increasing the "averaging effect" of individual pixels error on map predictions, thus potentially resulting in a "purest" signal at the 60-m stand level. Fourth, one cannot exclude the possibility that differences in the image quality, e.g. due to varying understanding of the impulse response, results in different effective spectral and radiometric resolution, which may have then contributed to differences in prediction accuracy.

The limit above which AGB can be inferred with passive sensors has been the subject of much discussion. For Landsat TM/ETM and OLI, many studies have shown a saturation point between 100 and 150 Mg ha^{-1} (Lu et al., 2016). To our knowledge, there have been only a few attempts to assess the saturation point in tropical forests with S2 and WV3 sensors. Here, using a large LiDAR dataset covering a broad forest structure gradient, we have shown that passive sensors do not convey reliable information above 200 Mg ha^{-1} for L8 and S2 data and above 250 Mg ha^{-1} for WV3 data. Depending on the type of sensor and the complexity of the vegetation structure, the saturation points may, however, differ. Thus, caution must be taken when transposing our saturation points to other study sites and forest types.

Texture analyses based on canopy characteristics in high to very high-resolution images have been previously shown to be good predictors of forest AGB without obvious saturation effects at high AGB values (Couteron et al., 2005, 2015; Ploton et al., 2012). In this study, although the first FOTO PCA axis was selected, it only modestly improved the model. Note also that taken individually, texture metrics did not correlate significantly with forest AGB (Fig. S8). The performance of such texture-based metrics to infer forest AGB has been shown to vary strongly among sites and forest types (Pargal et al., 2017; Ploton et al., 2017; Ploton et al., 2013) and to be highly dependent on image acquisition parameters (Barbier et al., 2011).

The problem of variable selection

The variables used to predict forest AGB vary strongly among studies in the literature, limiting cross-region comparisons (Brososke et al., 2014). Our robust automated procedure showed that no more than four to five variables should be retained for each sensor, from an initial set of 37 to 57 variables. For a few years now, the use of RF algorithm has become a standard approach in the field of RS. RF accounts for non-linear and interaction effects among predictors but at the same time, may be prone to overfitting (Xu et al., 2016). Despite this well-known limitation, previous studies have used a plethora of predictors (e.g., up to 24 in Pandit et al., 2018; 23 in

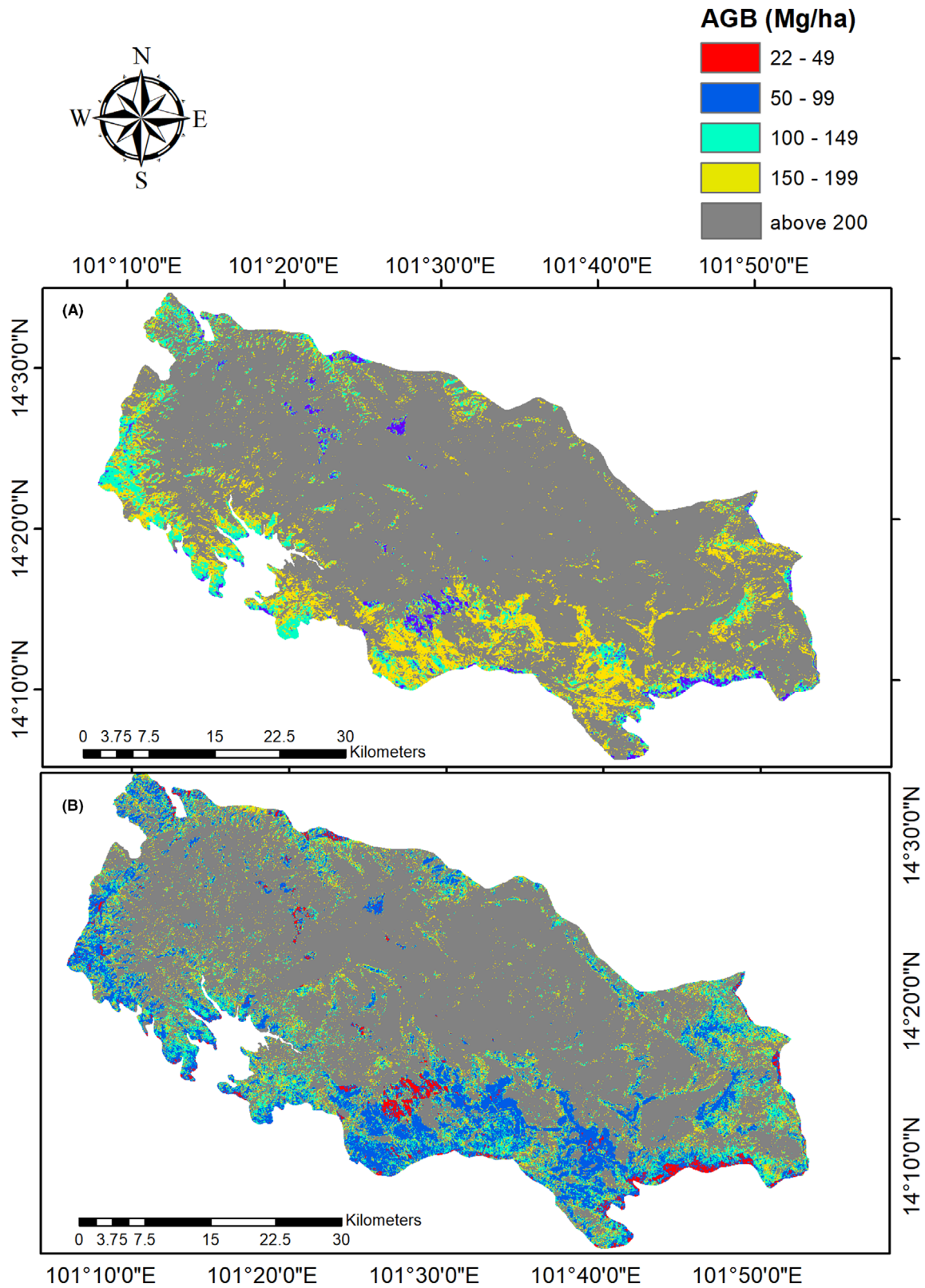


Figure 6. Extrapolated AGB values over the whole Khao Yai area using (A). Landsat-8 and B. Sentinel-2 selected models. As suggested by our results, AGB estimates $>200 \text{ Mg ha}^{-1}$ are considered as unreliable here and hence represented in an open class displayed in dark grey.

López-Serrano et al., 2016; 13 in Chen et al., 2019; 28 in López-Serrano et al., 2020) in RF model, with no robust selection procedure. We have shown here that simple models, accounting for no more than five RS predictors, performed at least as well as more complex models and that these simple models should be preferred based on the parsimony principle, even if no detrimental effects of overfitting were detected here (i.e., no increase in RMSE with more complex models; Fig. 2 and Fig. S5).

We have also shown that the selected predictors vary strongly from one sensor to another. The best AGB predictors were the Green_{0.560} band for L8, the Red-edge_{0.705} band for S2, and the NDRE index for WV3. Only the WDRVI index was commonly retained for L8 and S2. We also showed that the selection procedure favoured different predictors according to the range of AGB values considered (below and above 200 Mg ha⁻¹). However, the selection of variables can be slightly affected by the acquisition conditions, such as the period at which data were acquired, even if additional tests using L8 data acquired in May 2018 resulted in a similar AGB prediction error (Fig. S9). Note also that fusing all satellite data within a single model did not lead to any improvement, suggesting that these data bring little complementary information (Fig. S10). Lastly, when predictors were selected according to their transferability among sensors (Fig. 5), the three best predictors were the untransformed Green, Blue and Red bands. These visible bands, especially Green and Blue, are highly sensitive to variation in reflectance due to photosynthetic properties and vegetation cover (Rullan-Silva et al., 2013) and hence are expected to convey relevant information on forest structure. Surprisingly, while most of the vegetation indices proposed to predict forest structure rely on the Red and NIR band, we found that this band appears to be less informative than the Green and Blue bands for forest AGB predictions (Table S2). However, visible untransformed bands are highly sensitive to atmospheric effects and hence should be used with caution or with adequate correction model, especially when analyzing temporal series.

Implications for tropical forest carbon maps

Several studies have produced forest carbon maps by extrapolating extensive field- or LiDAR-based AGB estimates on the basis of passive RS data (e.g., Asner et al., 2013; Baccini et al., 2017; Xu et al., 2017), among which some are considered as reference AGB maps for the tropics (Baccini et al., 2012; Saatchi et al., 2011). In a recent comment on the map produced by Baccini et al. (2017) and Hansen et al. (2019) stated that the mapping exercise overstated our current capabilities for mapping forest carbon stocks and dynamics in dense tropical forests. Our

present results, as well as the comparison of our LiDAR AGB estimates with global biomass maps (Fig. S11), confirm this statement and call for much care in the interpretation and use of published large scale tropical forest carbon and AGB maps. As an example, over the whole of KYNP area (ca. 216 770 ha), we were able to map with enough confidence only 28% of the forested area corresponding to patches with AGB below to 200 Mg ha⁻¹, because predictions above this threshold appeared largely unreliable (Fig. 4). Thus, current passive satellite products do have the potential to produce High Carbon Stock (HCS) classifications, providing that HCS forests can be considered as forests storing more than 100 Mg ha⁻¹ C, but cannot otherwise produce satisfactory continuous AGB maps in tropical forests due to a lack of sensitivity above 200 Mg ha⁻¹. Within the low AGB area (≤ 200 Mg ha⁻¹), L8 and S2 data led to fairly consistent predictions ($r = 0.73$; $P < 0.0001$), but with significant local discrepancies at the edge and in the south-east quadrant of the study area (Fig. S12), even if the lack of field or LiDAR data in this area did not allow us to check which predictions were the most accurate. However, if AGB gradients were globally well-captured, absolute AGB values were predicted to be 34% higher from L8 data than from S2 data, suggesting that potential bias may arise in the estimate of the total AGB stored, even in the low AGB forests of KYNP (11.81 and 18.02 Tg with S2 and L8 data, respectively). One possible explanation is that our LiDAR calibration area (i.e., about 3.2% of full KYNP) does not perfectly represent the full extrapolated area of KYNP, e.g., due to variations in topographical conditions and forest types, which may have generated different behaviours of S2 and L8 data and thus large discrepancies (Wilkes et al., 2015). Finally, as already shown by previous studies (e.g., Xu et al., 2017), we have demonstrated that when calibrated with the full AGB gradient, our algorithm strongly overestimates low AGB values (by 35%–57% for predicted values ≤ 200 Mg ha⁻¹). However, the bias in overall biomass prediction is much lower when the model is only calibrated in the low biomass domain, i.e., ≤ 200 Mg ha⁻¹, in all three sensors (Fig. S13). Thus, not only are large AGB values poorly predicted by passive multispectral sensors, but this failure also induces a systematic bias in low AGB predictions.

Conclusions

In this paper, using multi-source satellite sensor datasets, we assessed the potential to map AGB at large scale in a heterogeneous dense forest area. Our results indicate that when passive RS data are used to predict forest AGB, (1) difference in overall performance depends on the spatial resolution, quality of sensor and on the bands available

on the original satellite datasets, (2) extreme caution should be taken when interpreting large predicted AGB values, (3) a high uncertainty remains associated with small AGB values, even if the associated AGB gradients can be fairly well-captured, and (4) calibrating the model only within the range of AGB values that can actually be predicted minimizes the risk of induced bias. On a global scale, our study points to the fact that, while waiting for upcoming more AGB-oriented sensors, freely available Sentinel data, which have a greater potential than the widely used Landsat data, should be preferred to extrapolate AGB values, at least in low-AGB forests.

Acknowledgments

We gratefully thank the National Science and Technology Development Agency (Thailand) for supporting long-term monitoring of all forest plots, the Department of National Parks, Wildlife and Plant Conservation (DNP) that supported our research and Pierre Ploton for useful comments on an earlier draft. NJ benefitted from the French Eiffel Excellence Scholarship Program and a mobility grant from the IRD institute in the AMAP laboratory (9 months). NB, VG, RP and MRM were partly supported by the CarboShareAsia project funded by the French Ministry of Foreign Affairs under the PHC Bio Asia 2016 program and the 3DForMod project funded by ANR under the UE FACCE ERA-GAS 2017 program (ANR-17-EGAS-0002-01). We thank Airbus Defence and Space for allowing us to use the Overland software.

Author Contributions

NJ and MRM designed the study; NJ analyzed the data; NJ and MRM investigated the data and wrote the paper's first draft; All authors provided valuable feedback on analyses and the manuscript.

Conflict of Interest

The authors declare that there is no conflict of interest.

Data Availability Statement

The data that support the findings of this study are available on request from the corresponding author.

References

Asner, G.P., Mascaro, J., Anderson, C., Knapp, D.E., Martin, R.E., Kennedy-Bowdoin, T. et al. (2013) High-fidelity national carbon mapping for resource management and REDD+. *Carbon Balance and Management*, **8**(1), 7. <https://doi.org/10.1186/1750-0680-8-7>

- Avitabile, V., Baccini, A., Friedl, M.A. & Schullius, C. (2012) Capabilities and limitations of Landsat and land cover data for aboveground woody biomass estimation of Uganda. *Remote Sensing of Environment*, **117**, 366–380. <https://doi.org/10.1016/j.rse.2011.10.012>
- Avitabile, V., M. Herold, G. B. Heuvelink, S. L. Lewis, O. L. Phillips, G. P. Asner, et al. 2016. An integrated pan-tropical biomass map using multiple reference datasets. *Global change biology* **22**(4), 1406–1420.
- Baccini, A. & Asner, G.P. (2013) Improving pantropical forest carbon maps with airborne LiDAR sampling. *Carbon Management*, **4**(6), 591–600. <https://doi.org/10.4155/cmt.13.66>
- Baccini, A., Goetz, S.J., Walker, W.S., Laporte, N.T., Sun, M., Sulla-Menashe, D. et al. (2012) Estimated carbon dioxide emissions from tropical deforestation improved by carbon-density maps. *Nature Climate Change*, **2**(3), 182–185. <https://doi.org/10.1038/nclimate1354>
- Baccini, A., Laporte, N., Goetz, S.J., Sun, M. & Dong, H. (2008) A first map of tropical Africa's above-ground biomass derived from satellite imagery. *Environmental Research Letters*, **3**(4), 045011. <https://doi.org/10.1088/1748-9326/3/4/045011>
- Baccini, A., Walker, W., Carvalho, L., Farina, M., Sulla-Menashe, D. & Houghton, R.A. (2017) Tropical forests are a net carbon source based on aboveground measurements of gain and loss. *Science*, **358**(6360), 230–234. <https://doi.org/10.1126/science.aam5962>
- Baloloy, A.B., Blanco, A.C., Candido, C.G., Argamosa, R.J.L., Dumalag, J.B.L.C., Dimapilis, L.L.C. et al. (2018). Estimation of mangrove forest aboveground biomass using multispectral bands, vegetation indices and biophysical variables derived from optical satellite imageries: rapideye, planetscope and sentinel-2. *ISPRS Annals of Photogrammetry, Remote Sensing and Spatial Information Sciences*, **IV-3**, 29–36. <https://doi.org/10.5194/isprs-annals-IV-3-29-2018>
- Bannari, A., Morin, D., Bonn, F. & Huete, A.R. (1995) A review of vegetation indices. *Remote Sensing Reviews*, **13** (1–2), 95–120. <https://doi.org/10.1080/02757259509532298>
- Barbier, N., Proisy, C., Véga, C., Sabatier, D. & Coutron, P. (2011) Bidirectional texture function of high resolution optical images of tropical forest: an approach using LiDAR hillshade simulations. *Remote Sensing of Environment*, **115** (1), 167–179. <https://doi.org/10.1016/j.rse.2010.08.015>
- Bastin, J.-F., Barbier, N., Coutron, P., Adams, B., Shapiro, A., Bogaert, J. et al. (2014) Aboveground biomass mapping of African forest mosaics using canopy texture analysis: toward a regional approach. *Ecological Applications*, **24**(8), 1984–2001. <https://doi.org/10.1890/13-1574.1>
- Berninger, A., Lohberger, S., Stängel, M. & Siegert, F. (2018) SAR-based estimation of above-ground biomass and its changes in tropical forests of Kalimantan using L- and C-

- Band. *Remote Sensing*, **10**(6), 831. <https://doi.org/10.3390/rs10060831>
- Boutton, T.W., Tieszen, L.L. & Imbamba, S.K. (1988) Biomass dynamics of grassland vegetation in Kenya. *African Journal of Ecology*, **26**(2), 89–101. <https://doi.org/10.1111/j.1365-2028.1988.tb00960.x>
- Brockelman, W.Y., Nathalang, A. & Maxwell, J.F. (2017) *Mo Singto plot: Flora and ecology*. Bangkok: National Science and Technology Development Agency, and Department of National Parks.
- Broszofske, K.D., Froese, R.E., Falkowski, M.J. & Banskota, A. (2014) A review of methods for mapping and prediction of inventory attributes for operational forest management. *Forest Science*, **60**(4), 733–756. <https://doi.org/10.5849/forsci.12-134>
- Chang, J. & Shoshany, M. (2016) Mediterranean shrublands biomass estimation using Sentinel-1 and Sentinel-2. *IEEE International Geoscience and Remote Sensing Symposium (IGARSS)*, **2016**, 5300–5303. <https://doi.org/10.1109/IGARSS.2016.7730380>
- Chanthorn, W., Hartig, F. & Brockelman, W.Y. (2017) Structure and community composition in a tropical forest suggest a change of ecological processes during stand development. *Forest Ecology and Management*, **404**, 100–107. <https://doi.org/10.1016/j.foreco.2017.08.001>
- Chave, J., Réjou-Méchain, M., Búrquez, A., Chidumayo, E., Colgan, M.S., Delitti, W.B.C. et al. (2014) Improved allometric models to estimate the aboveground biomass of tropical trees. *Global Change Biology*, **20**(10), 3177–3190. <https://doi.org/10.1111/gcb.12629>
- Chen, L., Wang, Y., Ren, C., Zhang, B. & Wang, Z. (2019) Optimal combination of predictors and algorithms for forest above-ground biomass mapping from sentinel and SRTM data. *Remote Sensing*, **11**(4), 414. <https://doi.org/10.3390/rs11040414>
- Clevers, J.G.P.W. (2014) Beyond NDVI: extraction of biophysical variables from remote sensing imagery. In: Manakos, I. & Braun, M. (Eds.) *Land use and land cover mapping in Europe: practices & trends*. Netherlands: Springer, pp. 363–381. https://doi.org/10.1007/978-94-007-7969-3_22
- Coutron, P., Barbier, N., Deblauwe, V., Pélissier, R. & Ploton, P. (2015) Texture analysis of very high spatial resolution optical images as a way to monitor vegetation and forest biomass in the tropics. *Multi-Scale Forest Biomass Assessment and Monitoring in the Hindu Kush Himalayan Region: A Geospatial Perspective*. Special Science Publication. Nepal: The International Centre for Integrated Mountain Development (ICIMOD), pp. 157–164.
- Coutron, P., Pélissier, R., Nicolini, E.A. & Paget, D. (2005) Predicting tropical forest stand structure parameters from Fourier transform of very high-resolution remotely sensed canopy images. *Journal of Applied Ecology*, **42**(6), 1121–1128. <https://doi.org/10.1111/j.1365-2664.2005.01097.x>
- Feret, J.B. & Barbier, N. (2018) *S2 BOA reflectance in the context of tropical rainforest: preliminary illustration of the challenges for the extraction of vegetation properties*. Workshop for Sentinel-2 L2A MAJA products.
- Gao, B.-C. (1995) Normalized difference water index for remote sensing of vegetation liquid water from space. *Imaging Spectrometry*, **2480**, 225–236. <https://doi.org/10.1117/12.210877>
- Ghosh, S.M. & Behera, M.D. (2018) Aboveground biomass estimation using multi-sensor data synergy and machine learning algorithms in a dense tropical forest. *Applied Geography*, **96**, 29–40. <https://doi.org/10.1016/j.apgeog.2018.05.011>
- Gitelson, A. (2004) Wide dynamic range vegetation index for remote quantification of biophysical characteristics of vegetation. *Journal of Plant Physiology*, **161**, 165–173. <https://doi.org/10.1078/0176-1617-01176>
- Gitelson, A.A., Kaufman, Y.J. & Merzlyak, M.N. (1996) Use of a green channel in remote sensing of global vegetation from EOS-MODIS. *Remote Sensing of Environment*, **58**(3), 289–298.
- Gitelson, A.A., Keydan, G.P. & Merzlyak, M.N. (2006) Three-band model for noninvasive estimation of chlorophyll, carotenoids, and anthocyanin contents in higher plant leaves. *Geophysical Research Letters*, **33**(11), L11402. <https://doi.org/10.1029/2006GL026457>
- Hansen, M.C., Potapov, P. & Tyukavina, A. (2019) Comment on "Tropical forests are a net carbon source based on aboveground measurements of gain and loss." *Science (New York, N.Y.)*, **363**(6423), eaar3629. <https://doi.org/10.1126/science.aar3629>
- Horler, D.N.H., Dockray, M. & Barber, J. (1983) The red edge of plant leaf reflectance. *International Journal of Remote Sensing*, **4**(2), 273–288. <https://doi.org/10.1080/01431168308948546>
- Jenks, K.E., Chanteap, P., Kanda, D., Peter, C., Cutter, P., Redford, T. et al. (2011) Using relative abundance indices from camera-trapping to test wildlife conservation hypotheses – an example from Khao Yai National Park. *Thailand. Tropical Conservation Science*, **4**(2), 113–131. <https://doi.org/10.1177/194008291100400203>
- Jha, N., Tripathi, N.K., Chanthorn, W., Brockelman, W., Nathalang, A., Pélissier, R. et al. (2020) Forest aboveground biomass stock and resilience in a tropical landscape of Thailand. *Biogeosciences*, **17**(1), 121–134. <https://doi.org/10.5194/bg-17-121-2020>
- Joshi, N., Mitchard, E.T.A., Brolly, M., Schumacher, J., Fernández-Landa, A., Johannsen, V.K. et al. (2017) Understanding ‘saturation’ of radar signals over forests. *Scientific Reports*, **7**, 1–11. <https://doi.org/10.1038/s41598-017-03469-3>
- Keeler, K.M., Bunnell, D.B., Diana, J.S., Adams, J.V., Mychek-Londer, J.G., Warner, D.M. et al. (2015) Evaluating the importance of abiotic and biotic drivers on Bythotrepes

- biomass in Lakes Superior and Michigan. *Journal of Great Lakes Research*, **41**, 150–160. <https://doi.org/10.1016/j.jglr.2015.07.010>
- Li, B., Wang, W., Bai, L., Chen, N. & Wang, W. (2019) Estimation of aboveground vegetation biomass based on Landsat-8 OLI satellite images in the Guanzhong Basin, China. *International Journal of Remote Sensing*, **40**(10), 3927–3947. <https://doi.org/10.1080/01431161.2018.1553323>
- Liaw, A. & Wiener, M. (2002) Classification and regression by randomForest. *R News*, **2**(3), 18–22.
- López-Serrano, P.M., Cárdenas Domínguez, J.L., Corral-Rivas, J.J., Jiménez, E., López-Sánchez, C.A. & Vega-Nieva, D.J. (2020) Modeling of aboveground biomass with Landsat 8 OLI and machine learning in temperate forests. *Forests*, **11**(1), 11. <https://doi.org/10.3390/f11010011>
- López-Serrano, P.M., López-Sánchez, C.A., Álvarez-González, J.G. & García-Gutiérrez, J. (2016) A comparison of machine learning techniques applied to Landsat-5 TM spectral data for biomass estimation. *Canadian Journal of Remote Sensing*, **42**(6), 690–705. <https://doi.org/10.1080/07038992.2016.1217485>
- Lu, D., Chen, Q., Wang, G., Liu, L., Li, G. & Moran, E. (2016) A survey of remote sensing-based aboveground biomass estimation methods in forest ecosystems. *International Journal of Digital Earth*, **9**(1), 63–105. <https://doi.org/10.1080/17538947.2014.990526>
- Lymburner, L., Beggs, P.J. & Jacobson, C. (2000) Estimation of canopy-average surface-specific leaf area using Landsat TM data. *Photogrammetric Engineering & Remote Sensing*. American Society for Photogrammetry and Remote Sensing, **66**, 2 edn, pp. 183–191.
- Malenovský, Z., Rott, H., Cihlar, J., Schaepman, M.E., García-Santos, G., Fernandes, R. et al. (2012) Sentinels for science: potential of Sentinel-1, -2, and -3 missions for scientific observations of ocean, cryosphere, and land. *Remote Sensing of Environment*, **120**, 91–101. <https://doi.org/10.1016/j.rse.2011.09.026>
- Marvin, D.C., Asner, G.P., Knapp, D.E., Anderson, C.B., Martin, R.E., Sinca, F. et al. (2014) Amazonian landscapes and the bias in field studies of forest structure and biomass. *Proceedings of the National Academy of Sciences of the United States of America*, **111**(48), E5224–E5232. <https://doi.org/10.1073/pnas.1412999111>
- Mascaro, J., Asner, G.P., Knapp, D.E., Kennedy-Bowdoin, T., Martin, R.E., Anderson, C. et al. (2014) A tale of two "Forests": random forest machine learning aids tropical forest carbon mapping. *PLoS One*, **9**(1), e85993. <https://doi.org/10.1371/journal.pone.0085993>
- Mascaro, J., Detto, M., Asner, G.P. & Muller-Landau, H.C. (2011) Evaluating uncertainty in mapping forest carbon with airborne LiDAR. *Remote Sensing of Environment*, **115**(12), 3770–3774. <https://doi.org/10.1016/j.rse.2011.07.019>
- McFeeters, S.K. (1996) The use of the Normalized Difference Water Index (NDWI) in the delineation of open water features. *International Journal of Remote Sensing*, **17**(7), 1425–1432. <https://doi.org/10.1080/01431169608948714>
- Mermoz, S., Réjou-Méchain, M., Villard, L., Le Toan, T., Rossi, V. & Gourlet-Fleury, S. (2015) Decrease of L-band SAR backscatter with biomass of dense forests. *Remote Sensing of Environment*, **159**, 307–317. <https://doi.org/10.1016/j.rse.2014.12.019>
- Meyer, V., Saatchi, S., Ferraz, A., Xu, L., Duque, A., García, M. et al. (2019) Forest degradation and biomass loss along the Chocó region of Colombia. *Carbon Balance and Management*, **14**(1), 2. <https://doi.org/10.1186/s13021-019-0117-9>
- Miller, J.D. & Thode, A.E. (2007) Quantifying burn severity in a heterogeneous landscape with a relative version of the delta Normalized Burn Ratio (dNBR). *Remote Sensing of Environment*, **109**(1), 66–80. <https://doi.org/10.1016/j.rse.2006.12.006>
- Mitchard, E.T., Saatchi, S.S., Baccini, A., Asner, G.P., Goetz, S.J., Harris, N.L. et al. (2013) Uncertainty in the spatial distribution of tropical forest biomass: a comparison of pan-tropical maps. *Carbon Balance and Management*, **8**(1), 10. <https://doi.org/10.1186/1750-0680-8-10>
- Mutanga, O. & Skidmore, A.K. (2004) Narrow band vegetation indices overcome the saturation problem in biomass estimation. *International Journal of Remote Sensing*, **25**(19), 3999–4014. <https://doi.org/10.1080/01431160310001654923>
- Pan, Y., Birdsey, R.A., Fang, J., Houghton, R., Kauppi, P.E., Kurz, W.A. et al. (2011). A large and persistent carbon sink in the world's forests. *Science*. **333**(6045), 988–993. <https://doi.org/10.1126/science.1201609>
- Pandit, S., Tsuyuki, S. & Dube, T. (2018) Landscape-scale aboveground biomass estimation in buffer zone community forests of central Nepal: coupling in situ measurements with Landsat 8 Satellite Data. *Remote Sensing*, **10**(11), 1848. <https://doi.org/10.3390/rs10111848>
- Pargal, S., Fararoda, R., Rajashekar, G., Balachandran, N., Réjou-Méchain, M., Barbier, N. et al. (2017) Inverting aboveground biomass-canopy texture relationships in a landscape of forest mosaic in the Western Ghats of India using very high resolution cartosat imagery. *Remote Sensing*, **9**(3), 228. <https://doi.org/10.3390/rs9030228>
- Ploton, P., Barbier, N., Couteron, P., Antin, C.M., Ayyappan, N., Balachandran, N. et al. (2017) Toward a general tropical forest biomass prediction model from very high resolution optical satellite images. *Remote Sensing of Environment*, **200**, 140–153. <https://doi.org/10.1016/j.rse.2017.08.001>
- Ploton, P., Barbier, N., Takoudjou Momo, S., Réjou-Méchain, M., Boyemba Bosela, F., Chuyong, G. et al. (2016) Closing a gap in tropical forest biomass estimation: taking crown mass variation into account in pantropical allometries. *Biogeosciences*, **13**, 1571–1585. <https://doi.org/10.5194/bg-13-1571-2016>

- Ploton, P., Mortier, F., Réjou-Méchain, M., Barbier, N., Picard, N., Rossi, V. et al. (2020) Spatial validation reveals poor predictive performance of large-scale ecological mapping models. *Nature Communications*, **11**(1), 4540. <https://doi.org/10.1038/s41467-020-18321-y>
- Ploton, P., Pélissier, R., Barbier, N., Proisy, C., Ramesh, B.R. & Coutron, P. (2013) Canopy texture analysis for large-scale assessments of tropical forest stand structure and biomass. In: Lowman, M., Devy, S. & Ganesh, T. (Eds.), *Treetops at risk: challenges of global canopy ecology and conservation*. Springer, pp. 237–245. https://doi.org/10.1007/978-1-4614-7161-5_24
- Ploton, P., Pélissier, R., Proisy, C., Flavenot, T., Barbier, N., Rai, S. et al. (2012) Assessing aboveground tropical forest biomass using Google Earth canopy images. *Ecological Applications: A Publication of the Ecological Society of America*, **22**, 993–1003. <https://doi.org/10.2307/23213933>
- Pu, R., Gong, P. & Yu, Q. (2008) Comparative analysis of EO-1 ALI and hyperion, and Landsat ETM+ data for mapping forest crown closure and leaf area index. *Sensors*, **8**(6), 3744–3766. <https://doi.org/10.3390/s8063744>
- Réjou-Méchain, M., Barbier, N., Coutron, P., Ploton, P., Vincent, G., Herold, M. et al. (2019) Upscaling forest biomass from field to satellite measurements: sources of errors and ways to reduce them. *Surveys in Geophysics*, **40**(4), 881–911. <https://doi.org/10.1007/s10712-019-09532-0>
- Réjou-Méchain, M., Muller-Landau, H.c., Detto, M., Thomas, S.c., Le Toan, T., Saatchi, S.S. et al. (2014) Local spatial structure of forest biomass and its consequences for remote sensing of carbon stocks. *Biogeosciences*, **11**, 6827–6840. <https://doi.org/10.5194/bg-11-6827-2014>
- Réjou-Méchain, M., Tanguy, A., Piponiot, C., Chave, J. & Hérault, B. (2017) biomass: an R package for estimating above-ground biomass and its uncertainty in tropical forests. *Methods in Ecology and Evolution*, **8**(9), 1163–1167. <https://doi.org/10.1111/2041-210X.12753>
- Roberts, D.R., Bahn, V., Ciuti, S., Boyce, M.S., Elith, J., Guillerma-Arroita, G. et al. (2017) Cross-validation strategies for data with temporal, spatial, hierarchical, or phylogenetic structure. *Ecography*, **40**(8), 913–929. <https://doi.org/10.1111/ecog.02881>
- Rodríguez, E., Morris, C.S. & Belz, J.E. (2006) A global assessment of the SRTM performance. *Photogrammetric Engineering & Remote Sensing*, **72**(3), 249–260 <https://doi.org/10.14358/PERS.72.3.249>
- Rullan-Silva, C.D., Olthoff, A.E., de la Mata, J.A.D. & Pajares-Alonso, J.A. (2013) Remote monitoring of forest insect defoliation -a review. *Forest Systems*, **22**(3), 377–391. <https://doi.org/10.5424/fs/2013223-04417>
- Saatchi, S.S., Harris, N.L., Brown, S., Lefsky, M., Mitchard, E.T.A., Salas, W. et al. (2011) Benchmark map of forest carbon stocks in tropical regions across three continents. *Proceedings of the National Academy of Sciences of the United States of America*, **108**(24), 9899–9904. <https://doi.org/10.1073/pnas.1019576108>
- Sagang, L.B.T., Ploton, P., Sonké, B., Poilvé, H., Coutron, P. & Barbier, N. (2020) Airborne lidar sampling pivotal for accurate regional agb predictions from multispectral images in forest-savanna landscapes. *Remote Sensing*, **12**(10), 1637. <https://doi.org/10.3390/rs12101637>
- Santoro, M., Beaudoin, A., Beer, C., Cartus, O., Fransson, J. E., Hall, R. J., et al. (2015) Forest growing stock volume of the northern hemisphere: Spatially explicit estimates for 2010 derived from Envisat ASAR. *Remote Sensing of Environment*, **168**, 316–334.
- Silva, C., Hudak, A., Vierling, L., Klauber, C., Garcia, M., Ferraz, A. et al. (2017) Impacts of airborne lidar pulse density on estimating biomass stocks and changes in a selectively logged tropical forest. *Remote Sensing*, **9**(10), 1068. <https://doi.org/10.3390/rs9101068>
- Sims, D.A. & Gamon, J.A. (2002) Relationships between leaf pigment content and spectral reflectance across a wide range of species, leaf structures and developmental stages. *Remote Sensing of Environment*, **81**(2), 337–354. [https://doi.org/10.1016/S0034-4257\(02\)00010-X](https://doi.org/10.1016/S0034-4257(02)00010-X)
- Tucker, C.J. (1979) Red and photographic infrared linear combinations for monitoring vegetation. *Remote Sensing of Environment*, **8**(2), 127–150. [https://doi.org/10.1016/0034-4257\(79\)90013-0](https://doi.org/10.1016/0034-4257(79)90013-0)
- Tuominen, S. & Pekkarinen, A. (2005) Performance of different spectral and textural aerial photograph features in multi-source forest inventory. *Remote Sensing of Environment*, **94**(2), 256–268. <https://doi.org/10.1016/j.rse.2004.10.001>
- Vincini, M., Frazzi, E. & D'Alessio, P. (2008) A broad-band leaf chlorophyll vegetation index at the canopy scale. *Precision Agriculture*, **9**(5), 303–319. <https://doi.org/10.1007/s11119-008-9075-z>
- Wang, F., Huang, J., Tang, Y. & Wang, X. (2007) New vegetation index and its application in estimating leaf area index of rice. *Rice Science*, **14**(3), 195–203. [https://doi.org/10.1016/S1672-6308\(07\)60027-4](https://doi.org/10.1016/S1672-6308(07)60027-4)
- Widłowski, J.-L., Pinty, B., Gobron, N., Verstraete, M.M., Diner, D.J. & Davis, A.B. (2004) Canopy structure parameters derived from multi-angular remote sensing data for terrestrial carbon studies. *Climatic Change*, **67**(2), 403–415. <https://doi.org/10.1007/s10584-004-3566-3>
- Wilkes, P., Jones, S., Suarez, L., Mellor, A., Woodgate, W., Soto-Berelov, M. et al. (2015) Mapping forest canopy height across large areas by upscaling ALS estimates with freely available satellite data. *Remote sensing*, **7**(9), 12563–12587.
- Xu, L., Saatchi, S.S., Shapiro, A., Meyer, V., Ferraz, A., Yang, Y. et al. (2017) Spatial distribution of carbon stored in forests of the democratic republic of Congo. *Scientific Reports*, **7**(1), 1–12. <https://doi.org/10.1038/s41598-017-15050-z>

- Xu, L., Saatchi, S.S., Yang, Y., Yu, Y. & White, L. (2016) Performance of non-parametric algorithms for spatial mapping of tropical forest structure. *Carbon Balance and Management*, **11** (1), 18. <https://doi.org/10.1186/s13021-016-0062-9>
- Zhang, C., Ren, H., Qin, Q. & Ersoy, O.K. (2017) A new narrow band vegetation index for characterizing the degree of vegetation stress due to copper: the copper stress vegetation index (CSVI). *Remote Sensing Letters*, **8**(6), 576–585. <https://doi.org/10.1080/2150704X.2017.1306135>.
- Zhao, P., Lu, D., Wang, G., Wu, C., Huang, Y. & Yu, S. (2016) Examining Spectral reflectance saturation in Landsat imagery and corresponding solutions to improve forest aboveground biomass estimation. *Remote Sensing*, **8**(6), 469. <https://doi.org/10.3390/rs8060469>
- Zolkos, S.G., Goetz, S.J. & Dubayah, R. (2013) A meta-analysis of terrestrial aboveground biomass estimation using lidar remote sensing. *Remote Sensing of Environment*, **128**, 289–298. <https://doi.org/10.1016/j.rse.2012.10.017>

Supporting Information

Additional supporting information may be found online in the Supporting Information section at the end of the article.

Figure S1. Spatial Variogram of illustrate the spatial autocorrelation of the LiDAR AGB. The distance is in meters.

Figure S2. Scatter density plots between the selected predictors of Landsat-8 individually with AGB_{LIDAR} . (A) $Green_{0.560}$; (B) $Blue_{0.483}$; (C) WDRVI; (D) CVI. Blue to red color indicates low to high point density, respectively.

Figure S3. Scatter density plots between the selected predictors of Sentinel-2 individually with AGB_{LIDAR} . (A) $Red-edge_{1.0705}$ band; (B) WDRVI; (C) MI; (D) NDWI. Blue to red color indicates low to high point density, respectively.

Figure S4. Scatter density plots between the selected predictors of Worldview-3 individually with AGB_{LIDAR} . (A) NDRE (B) GVIMSS (C) Cgreen (D) FotoPCA1 E.LCI. Blue to red color indicates low to high point density, respectively.

Figure S5. Selection of the best predictors of LiDAR-derived AGB values below or equal to (A, B, and C) and above (D, E and F) an arbitrary threshold AGB of 200 Mg ha^{-1} for three multi-spectral satellite sensors using leave-one-block-out (LOBO) cross-validation approach with a forward selection approach.

Figure S6. Scatter density plots between the best predictors of different sensors for predicting AGB_{LIDAR} value below or equal to 200 Mg ha^{-1} (A) Landsat-8 $Green_{0.560}$ Band (B) Sentinel-2 $Red-edge_{1.0705}$ Band C.

Figure S7. Scatter density plots between the best predictors of different sensors for predicting AGB_{LIDAR} value above 200 Mg ha^{-1} (A) Landsat-8 $Green_{0.560}$ Band (B) Sentinel-2 GVIMSS (C) Worldview-3 $Red-edge_{1.0725}$ Band with $AGB_{LIDAR} > 200 \text{ Mg ha}^{-1}$.

Figure S8. Scatter density plots between the texture variables of Worldview 3 with AGB_{LIDAR} (A–C) FotoPCA1-3 (D–F) LacuPCA1-PCA3. Blue to red color indicates low to high point density, respectively.

Figure S9. Selection of sensor predictors using both a leave-one-block-out (LOBO) cross-validation approach and a forward selection for Landsat 8 data acquired in May 2018.

Figure S10. Selection of sensor predictors using both a leave-one-block-out (LOBO) cross-validation approach and a forward selection for the three satellite datasets combined together.

Figure S11. The performance of several published global and pan-tropical biomass maps to predict LiDAR-AGB estimates in our study area with (A) The integrated pantropical biomass map by Avitabile et al. (2016); (B) Global forest biomass GEOCARBON based on Avitabile et al. (2016) and Santoro et al. (2015); (C) The pantropical Baccini et al. (2012) map (most of our study area was covered with cloud and hence masked out in their map) (D) The pantropical Saatchi et al. (2011) map.

Figure S12. The arithmetic difference (pixel by pixel) between Landsat 8 predicted AGB and Sentinel 2 predicted AGB. The AGB estimates $> 200 \text{ Mg ha}^{-1}$ would be unreliable as shown in our study case, and hence threshold has been set to 200 Mg ha^{-1} (above threshold denoted by dark gray).

Figure S13. Bias comparison for the low AGB values with the complete calibration model (all AGB values; shown in Left column A,C,E) and with the model calibration restricted to low AGB values ($\leq 200 \text{ Mg ha}^{-1}$; shown in Right column B,D,F).

Table S1. Accuracy estimates and saturation point values found in the present study for the three studied sensors.

Table S2. Correlation between individual Blue, Green, Red and NIR bands from the three sensors with LiDAR AGB estimates.